LETTER

doi:10.1038/nature24623

Blazar spectral variability as explained by a twisted inhomogeneous jet

C. M. Raiteri[1], M. Villata[1], J. A. Acosta-Pulido[2,3], I. Agudo[4], A. A. Arkharov[5], R. Bachev[6], G. V. Baida[7], E. Benítez[8], G. A. Borman[7], W. Boschin[2,3,9], V. Bozhilov[10], M. S. Butuzova[7], P. Calcidese[11], M. I. Carnerero[1], D. Carosati[9,12], C. Casadio[4,13], N. Castro-Segura[3,14], W.-P. Chen[15], G. Damljanovic[16], F. D'Ammando[17,18], A. Di Paola[19], J. Echevarría[8], N. V. Efimova[5], Sh. A. Ehgamberdiev[20], C. Espinosa[8], A. Fuentes[4], A. Giunta[19], J. L. Gómez[4], T. S. Grishina[21], M. A. Gurwell[22], D. Hiriart[8], H. Jermak[23], B. Jordan[24], S. G. Jorstad[21,25], M. Joshi[25], E. N. Kopatskaya[21], K. Kuratov[26,27], O. M. Kurtanidze[28,29,30,31], S. O. Kurtanidze[28], A. Lähteenmäki[32,33,34], V. M. Larionov[5,21], E. G. Larionova[21], L. V. Larionova[21], C. Lázaro[2,3], C. S. Lin[15], M. P. Malmrose[25], A. P. Marscher[25], K. Matsumoto[35], B. McBreen[36], R. Michel[8], B. Mihov[6], M. Minev[10], D. O. Mirzaqulov[20], A. A. Mokrushina[5,21], S. N. Molina[4], J. W. Moody[37], D. A. Morozova[21], S. V. Nazarov[7], M. G. Nikolashvili[28], J. M. Ohlert[38,39], D. N. Okhmat[7], E. Ovcharov[10], F. Pinna[2,3], T. A. Polakis[40], C. Protasio[2,3], T. Pursimo[41], F. J. Redondo-Lorenzo[2,3], N. Rizzi[42], G. Rodriguez-Coira[2,3], K. Sadakane[35], A. C. Sadun[43], M. R. Samal[15], S. S. Savchenko[21], E. Semkov[6], B. A. Skiff[44], L. Slavcheva-Mihova[6], P. S. Smith[45], I. A. Steele[23], A. Strigachev[6], J. Tammi[32], C. Thum[46], M. Tornikoski[32], Yu. V. Troitskaya[21], I. S. Troitsky[21], A. A. Vasilyev[21] & O. Vince[16]

Blazars are active galactic nuclei, which are powerful sources of radiation whose central engine is located in the core of the host galaxy. Blazar emission is dominated by non-thermal radiation from a jet that moves relativistically towards us, and therefore undergoes Doppler beaming[1]. This beaming causes flux enhancement and contraction of the variability timescales, so that most blazars appear as luminous sources characterized by noticeable and fast changes in brightness at all frequencies. The mechanism that produces this unpredictable variability is under debate, but proposed mechanisms include injection, acceleration and cooling of particles[2], with possible intervention of shock waves[3,4] or turbulence[5]. Changes in the viewing angle of the observed emitting knots or jet regions have also been suggested as an explanation of flaring events[6–10] and can also explain specific properties of blazar emission, such as intra-day variability[11], quasi-periodicity[12,13] and the delay of radio flux variations relative to optical changes[14]. Such a geometric interpretation, however, is not universally accepted because alternative explanations based on changes in physical conditions—such as the size and speed of the emitting zone, the magnetic field, the number of emitting particles and their energy distribution—can explain snapshots of the spectral behaviour of blazars in many cases[15,16]. Here we report the results of optical-to-radio-wavelength monitoring of the blazar CTA 102 and show that the observed long-term trends of the flux and spectral variability are best explained by an inhomogeneous, curved jet that undergoes changes in orientation over time. We propose that magnetohydrodynamic instabilities[17] or rotation of the twisted jet[6] cause different jet regions to change their orientation and hence their relative Doppler factors. In particular, the extreme optical outburst of 2016–2017 (brightness increase of six magnitudes) occurred when the corresponding jet-emitting region had a small viewing angle. The agreement between observations and theoretical predictions can be seen as further validation of the relativistic beaming theory.

The blazar CTA 102 belongs to the subclass of flat-spectrum radio quasars (FSRQs). Its redshift, $z = 1.037$, corresponds to a luminosity distance of about 7,000 Mpc (assuming a flat Universe and a Hubble constant $H_0 = 70\,\mathrm{km\,s^{-1}\,Mpc^{-1}}$).

The Whole Earth Blazar Telescope (WEBT) Collaboration started to monitor the multiwavelength behaviour of CTA 102 in 2008. Data obtained until January 2013 are reported in ref. 9. In Extended Data Fig. 1 we show the optical and near-infrared light curves acquired in 2013–2017, which were built with data from 39 telescopes in 28 observatories, and in Methods we give some details on these observations.

A period of relatively low activity was recently interrupted by a sudden increase in the source brightness in late 2016, with a jump of 6–7 magnitudes with respect to the minima in the optical and near-infrared bands. The peak of the outburst was observed on 28 December 2016, with an R-band magnitude of 10.82 ± 0.04 (see Fig. 1), which corresponds to a luminosity L_ν at frequency ν of $\log[\nu L_\nu\,(\mathrm{erg\,s^{-1}})] = 48.12$

[1]INAF, Osservatorio Astrofisico di Torino, I-10025 Pino Torinese, Italy. [2]Instituto de Astrofisica de Canarias (IAC), La Laguna, E-38200 Tenerife, Spain. [3]Departamento de Astrofisica, Universidad de La Laguna, La Laguna, E-38205 Tenerife, Spain. [4]Instituto de Astrofísica de Andalucía (CSIC), E-18080 Granada, Spain. [5]Pulkovo Observatory, 196140 St Petersburg, Russia. [6]Institute of Astronomy and NAO, Bulgarian Academy of Sciences, 1784 Sofia, Bulgaria. [7]Crimean Astrophysical Observatory RAS, Nauchny 298409, Russia. [8]Instituto de Astronomía, Universidad Nacional Autónoma de México, Mexico. [9]INAF, TNG Fundación Galileo Galilei, E-38712 La Palma, Spain. [10]Department of Astronomy, Faculty of Physics, University of Sofia, BG-1164 Sofia, Bulgaria. [11]Osservatorio Astronomico della Regione Autonoma Valle d'Aosta, I-11020 Nus, Italy. [12]EPT Observatories, Tijarafe, E-38780 La Palma, Spain. [13]Max-Planck-Institut für Radioastronomie, D–53121 Bonn, Germany. [14]School of Physics and Astronomy, University of Southampton, Southampton SO17 1BJ, UK. [15]Graduate Institute of Astronomy, National Central University, Jhongli City, Taoyuan County 32001, Taiwan. [16]Astronomical Observatory, 11060 Belgrade, Serbia. [17]Dipartimento di Fisica e Astronomia, Università di Bologna, I-40129 Bologna, Italy. [18]INAF, Istituto di Radioastronomia, I-40129 Bologna, Italy. [19]INAF, Osservatorio Astronomico di Roma, I-00040 Monte Porzio Catone, Italy. [20]Ulugh Beg Astronomical Institute, Maidanak Observatory, Tashkent 100052, Uzbekistan. [21]Astronomical Institute, St Petersburg State University, 198504 St Petersburg, Russia. [22]Harvard-Smithsonian Center for Astrophysics, Cambridge, Massachusetts 02138, USA. [23]Astrophysics Research Institute, Liverpool John Moores University, Liverpool L3 5RF, UK. [24]School of Cosmic Physics, Dublin Institute For Advanced Studies, Dublin, Ireland. [25]Institute for Astrophysical Research, Boston University, Boston, Massachusetts 02215, USA. [26]NNLOT, Al-Farabi Kazakh National University, Almaty, Kazakhstan. [27]Fesenkov Astrophysical Institute, Almaty, Kazakhstan. [28]Abastumani Observatory, Mt Kanobili, 0301 Abastumani, Georgia. [29]Engelhardt Astronomical Observatory, Kazan Federal University, Tatarstan, Russia. [30]Landessternwarte, Zentrum für Astronomie der Universität Heidelberg, 69117 Heidelberg, Germany. [31]Center for Astrophysics, Guangzhou University, Guangzhou 510006, China. [32]Aalto University Metsähovi Radio Observatory, FI-02540 Kylmälä, Finland. [33]Aalto University Department of Electronics and Nanoengineering, FI-00076 Aalto, Finland. [34]Tartu Observatory, 61602 Tõravere, Estonia. [35]Astronomical Institute, Osaka Kyoiku University, Osaka 582-8582, Japan. [36]School of Physics, University College Dublin, Dublin 4, Ireland. [37]Department of Physics and Astronomy, Brigham Young University, Provo, Utah 84602, USA. [38]Michael Adrian Observatorium, Astronomie Stiftung Trebur, 65468 Trebur, Germany. [39]University of Applied Sciences, Technische Hochschule Mittelhessen, 61169 Friedberg, Germany. [40]Command Module Observatory, Tempe, Arizona, USA. [41]Nordic Optical Telescope, E-38700 Santa Cruz de La Palma, Spain. [42]Osservatorio Astronomico Sirio, I-70013 Castellana Grotte, Italy. [43]Department of Physics, University of Colorado Denver, Denver, Colorado 80217-3364 USA. [44]Lowell Observatory, Flagstaff, Arizona, USA. [45]Steward Observatory, University of Arizona, Tucson, Arizona, USA. [46]Instituto de Radio Astronomía Milimétrica, E-18012 Granada, Spain.

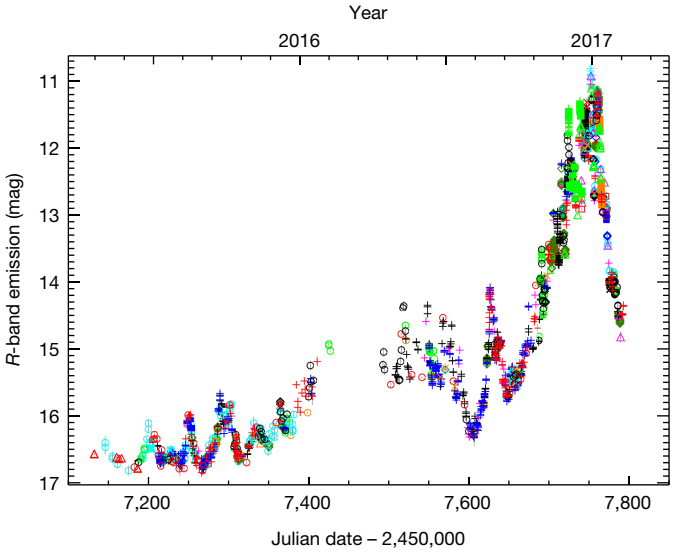

Figure 1 | Observed optical light curve of CTA 102 in the last two observing seasons of the WEBT campaign. *R*-band magnitudes are shown as a function of the Julian date (JD). Different colours and symbols correspond to the various telescopes contributing to the WEBT campaign. Error bars represent 1 s.d. measurement errors. The peak of the 2016–2017 outburst was observed on 28 December 2016 and indicates a brightness increase of about 6 mag with respect to the faintest state.

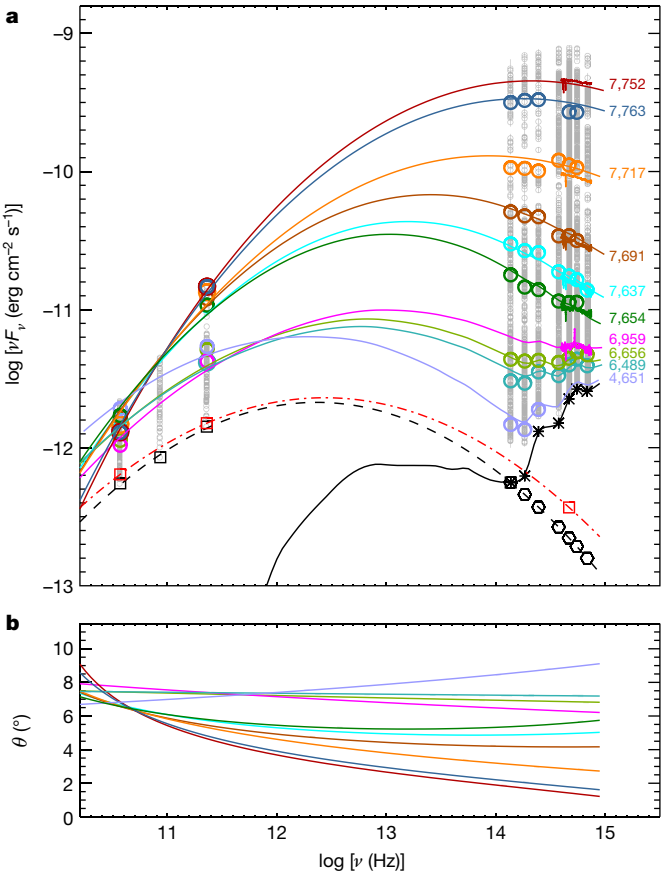

Figure 2 | Spectral energy distributions of CTA 102 and orientation of the emitting regions of the jet. a, Small grey circles highlight the observed variability ranges. The black dashed line represents the minimum-brightness synchrotron SED and the black squares (hexagons) the fitted (derived) minimum synchrotron flux densities. The black solid line and asterisks show the thermal emission model and its contributions to the near-infrared and optical bands. The red dot-dashed line represents the base-level synchrotron SED used for the geometric interpretation. Large coloured circles and coloured lines display observed data and spectra and model predictions, respectively, for selected epochs (expressed in JD − 2,450,000). Measurement errors (1 s.d.) are smaller than the symbol size. **b**, Viewing angles of the emitting region producing the (bulk of the) radiation at frequency ν at the epochs shown in **a**.

(corrected for the redshift effect, but without a beaming correction). This represents the most luminous optical blazar state ever detected. The previous record was held by the FSRQ 3C 454.3, which reached $\log[\nu L_\nu\,(\mathrm{erg\ s^{-1}})] = 47.54$ during a big outburst[18] observed in 2005.

Inspection of the light curves of CTA 102 reveals that the brightness variation amplitude is larger in the near-infrared than in the optical band. This is a consequence of the source emitting not only synchrotron radiation from the jet, but also thermal radiation from the accretion disk[19] that feeds the super-massive black hole of the active galactic nucleus (AGN). The more stable light from the disk makes a larger contribution to the overall source flux at optical wavelengths than in the near-infrared. Further evidence of thermal radiation from the disk comes from the analysis of colour indices and spectroscopic data (see Methods and Extended Data Figs 3 and 4).

To analyse the synchrotron emission from the jet, we first model the thermal component, usually referred to as the 'big blue bump' (BBB). Besides the disk radiation, the BBB includes the contribution of emission lines from the broad-line region of the AGN, in particular, Mg II and Hα lines, redshifted to the optical *V* and near-infrared *J* bands, respectively. In the BBB model (details in Methods), we built the spectral energy distribution (SED) of a hypothetical minimum-brightness synchrotron state and then subtracted it from the flux minima in all optical and near-infrared bands to get the BBB contribution. We also added a dust torus emission component in the mid- to far-infrared, as dust emission has been detected in CTA 102 with the IRAS[20] and Spitzer[21] satellites. The results are shown in Fig. 2.

Having modelled the thermal contribution to the source flux, we subtracted it from the near-infrared and optical flux densities to get the jet synchrotron flux. Figure 3 shows the optical *R* band, millimetre-wavelength (230 GHz) and radio (37 GHz) light curves in the period 2008–2017. The optical flux density of the jet ranges from 0.047 mJy to 166 mJy, with a maximum flux ratio higher than 3,500. We note that both the 2012 flare and the 2016–2017 outburst were accompanied by radio activity, but the flux ratios at the peaks of the two events are very different in the various bands. Moreover, in 2012, peaks at lower frequencies followed those at higher frequencies, as is often observed in blazars[14]. By contrast, the latest optical outburst was preceded by activity at 37 GHz. Figure 3 also shows that the high flux densities registered at 37 GHz in 2008–2009 correspond to a 'quiescent' optical state. This complex optical–radio correlation suggests that the emission in these two bands is produced in different regions of the jet. Explaining the multiwavelength light curves in terms of intrinsic processes would require very different physical conditions along the jet at various epochs, with model parameters chosen ad hoc at any time to reproduce the observed flux levels. Therefore, we propose an alternative scenario, in which the observed source behaviour is ascribed to orientation changes in the jet.

In the light curves of Figs 1 and 3 and Extended Data Fig. 1, especially in the optical and near-infrared bands, we can distinguish fast flares superimposed on a long-term trend. We adopted cubic spline interpolations through the binned data to represent the long-term behaviour of the well-sampled light curves in the *R* band, at 230 GHz and 37 GHz. For the radio and millimetre-wavelength light curves, which are characterized by smooth variations, we used a fixed time bin of 30 days. In the optical band, the fast flares are more rapid and pronounced when the source is brighter. This is expected when the long-term trend is due to a variable Doppler factor δ, which affects both the amplitudes and the timescales of the flux variations. In Methods, we summarize the basic concepts of the relativistic beaming theory and verify the contraction of

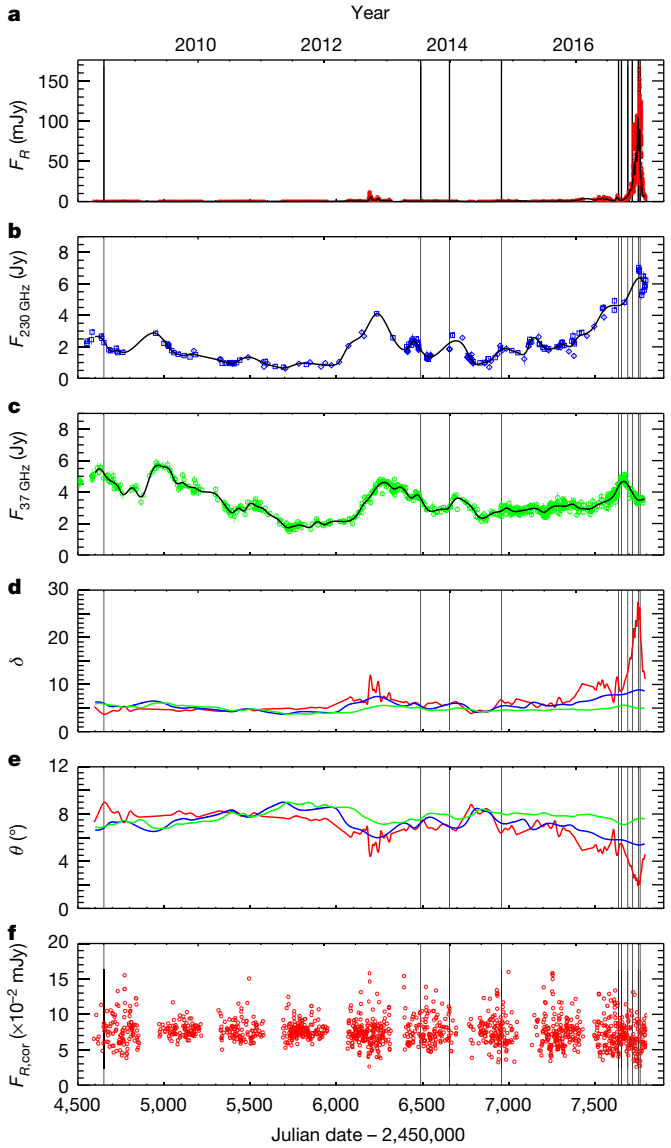

Figure 3 | Multifrequency behaviour of the jet emission of CTA 102 in 2008–2017. a–c, The *R*-band (**a**), 230-GHz (**b**) and 37-GHz (**c**) light curves contain 10,462, 170 and 576 flux density points, respectively. Error bars represent 1 s.d. measurement errors. Grey solid lines are cubic spline interpolations through the binned light curves. **d**, **e**, The Doppler factor δ (**d**) and viewing angle θ (**e**) of the optical (red), 230 GHz (blue) and 37 GHz (green) emitting regions according to the geometric model. **f**, *R*-band flux densities obtained for a constant $\delta = \delta_{base}$, namely, corrected for the variable beaming effect,. The vertical lines indicate the epochs considered in Fig. 2.

the flux variation timescales in the brightest optical states. Accordingly, we adopted a variable bin size ranging from 24 days in the low-flux states to 3.4 days in the phases of the 2016–2017 outburst with the most marked changes. The dispersion (root-mean-square) of the optical flux densities around the spline in the various observing seasons changed from 0.03 mJy to 1.1 mJy at the time of the 2012 flare and to 18 mJy during the 2016–2017 outburst. This confirms that fast flares are amplified during high-flux states and strongly indicates that long-term flux changes are probably due to variations in the Doppler factor.

If we accept this, then we can trace the behaviour of δ in time (see Fig. 3) at the three reference frequencies. Because of Doppler beaming, what we observe at a given frequency is emitted by the source at a lower frequency. To correct for this effect, we use the relativistic invariant F_ν/ν^2 (see, for example, ref. 22), where F_ν is the flux density at frequency ν. We build a base-level synchrotron spectrum for the long-term flux variations by fitting a log-parabolic model to the spline minima at 37 GHz, 230 GHz and in the *R* band (see Fig. 2). This is what we assume to be the source SED for the minimum Doppler factor δ_{base}. Starting from here, for each observed F_ν, we look for the corresponding frequency ν_{base} in the base-level spectrum so that $F_\nu(\nu)/\nu^2 = F_{\nu,base}(\nu_{base})/\nu^2_{base}$. Once ν_{base} is found, we can calculate the Doppler factor as $\delta = \delta_{base}(\nu/\nu_{base})$. The trends of δ shown in Fig. 3 were obtained assuming typical values[23] for the bulk Lorentz factor ($\Gamma = 20$) and for the maximum viewing angle ($\theta_{max} = 9°$) so that $\delta_{base} = 3.7$. Other choices for Γ and θ_{max} do not alter the general findings. The data constrain the ratio $\delta(t)/\delta_{base}$, whereas the choice of θ_{max} constrains Γ to yield a reasonable θ_{min}. In the light of what is known for blazars (for example, from the study of superluminal radio knots), values of θ_{max} between about 5° and 15°, which correspond to values of Γ between 35 and 10, are possible.

The Doppler factor depends on the bulk Lorentz factor and on the viewing angle. Although changes of Γ both along the jet (see Methods) and in time are in principle possible, they would require large differential accelerations or decelerations of the bulk flow in the various jet regions to explain the extreme flux changes in CTA 102. Instead, we favour the premise that Doppler factor variations are caused by orientation changes, which is also supported by the development of non-axisymmetric instabilities in magnetohydrodynamic jet simulations[17] and by very-long-baseline interferometry observations of CTA 102[24] and blazars with swirling jets[25] or helical jet structures[26] (although on much larger, parsec scales).

Having $\delta(t)$ and a guess for Γ, we can then derive the viewing angle as a function of time. This is shown in Fig. 3 for the three reference bands. Flux enhancements are seen at a given frequency when the corresponding jet-emitting region becomes better aligned with the line of sight. This is observed mainly in the optical band during the 2016–2017 outburst.

If we now correct the flux densities for the variable δ effect (see Methods), we obtain what we would observe if all the emitting regions of the jet had the same orientation, which does not change in time, that is, a constant δ. The residual variability corresponds to fast flares, which are probably caused by intrinsic, energetic processes. The fast flares show similar amplitudes over the whole 2008–2017 period. The dispersion factor in the various observing seasons is reduced to 2 (0.009–0.022 mJy), compared to the original factor of 600 that should be ascribed to energetic processes within the jet to explain the observed variability.

The above scenario implies that the emission at different frequencies comes from different regions along a continuous jet (that is, the jet is inhomogeneous), which have different orientations with respect to the line of sight that vary in time. A schematic representation of our model is given in Fig. 4.

The variations in θ, δ and the flux (Figs 2 and 3) have smaller amplitudes and are smoother in the radio- and millimetre-wavelength bands compared to those seen at shorter wavelengths. According to the model, this is probably due to the fact that the radio and millimetre-wavelength emitting regions are much more extended along the curved jet than those emitting optical and near-infrared light. Smaller variations would be expected from a larger emission region because the observed emission would be integrated, and thus averaged, over a greater span of angles with respect to the line of sight.

We tested the proposed geometric model by comparing predicted and observed SEDs (Fig. 2). For a given epoch, the predicted SED was obtained by summing the thermal emission model with a synchrotron SED derived by applying the Doppler enhancement to the base-level SED with a frequency-dependent $\delta(\nu)$ (details are given in Methods). The agreement between model and data is very good.

We also analysed optical polarimetric data (see Methods and Extended Data Fig. 6). The polarization fraction shows strong variability throughout the period considered but no general correlation

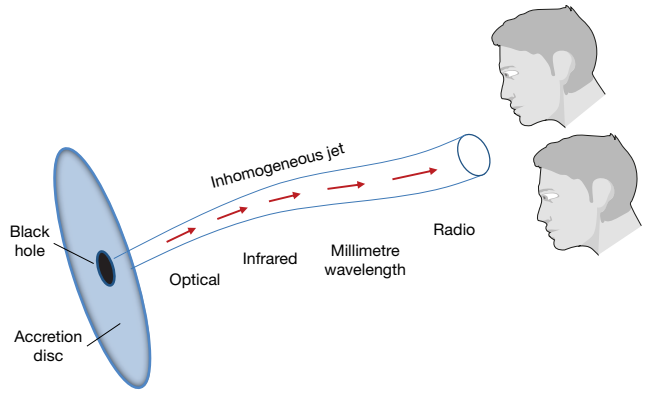

Figure 4 | Schematic representation of the proposed inhomogeneous jet model. Photons of different frequencies come from diverse jet regions. Because of the curvature of the jet, these regions have different orientations. Therefore, the corresponding emission is more (less) enhanced when the region is better (worse) aligned with the line of sight. The jet structure is dynamic, and the orientation of each region changes in time. The two observing eyes on the right represent two different alignments of the line of sight relative to the jet. The upper observer will see enhanced emission in the optical band and relatively low flux between the millimetre-wavelength and radio bands, while for the lower observer the most beamed radiation is the millimetre-wavelength one.

with the flux, suggesting a mainly stochastic process due to turbulence[5] or a variable jet direction[27]. On the other hand, the polarization angle undergoes large changes and in some cases its behaviour is consistent with the picture of a rotating twisted jet.

Online Content Methods, along with any additional Extended Data display items and Source Data, are available in the online version of the paper; references unique to these sections appear only in the online paper.

Received 22 June; accepted 6 October 2017.
Published online 4 December 2017.

1. Blandford, R. D. & Königl, A. Relativistic jets as compact radio sources. *Astrophys. J.* **232,** 34–48 (1979).
2. Ghisellini, G., Celotti, A. & Costamante, L. Low power BL Lacertae objects and the blazar sequence. Clues on the particle acceleration process. *Astron. Astrophys.* **386,** 833–842 (2002).
3. Marscher, A. P. & Gear, W. K. Models for high-frequency radio outbursts in extragalactic sources, with application to the early 1983 millimeter-to-infrared flare of 3C 273. *Astrophys. J.* **298,** 114–127 (1985).
4. Sikora, M., Błażejowski, M., Begelman, M. C. & Moderski, R. Modeling the production of flares in gamma-ray quasars. *Astrophys. J.* **554,** 1–11 (2001).
5. Marscher, A. P. Turbulent, extreme multi-zone model for simulating flux and polarization variability in blazars. *Astrophys. J.* **780,** 87 (2013).
6. Villata, M. & Raiteri, C. M. Helical jets in blazars I. The case of Mkn 501. *Astron. Astrophys.* **347,** 30–36 (1999).
7. Marscher, A. P. *et al.* The inner jet of an active galactic nucleus as revealed by a radio-to-gamma-ray outburst. *Nature* **452,** 966–969 (2008).
8. Abdo, A. A. *et al.* A change in the optical polarization associated with a γ-ray flare in the blazar 3C 279. *Nature* **463,** 919–923 (2010).
9. Larionov, V. M. *et al.* Exceptional outburst of the blazar CTA 102 in 2012: the GASP-WEBT campaign and its extension. *Mon. Not. R. Astron. Soc.* **461,** 3047–3056 (2016).
10. Casadio, C. *et al.* A multi-wavelength polarimetric study of the blazar CTA 102 during a gamma-ray flare in 2012. *Astrophys. J.* **813,** 51–64 (2015).
11. Camenzind, M. & Krockenberger, M. The lighthouse effect of relativistic jets in blazars. A geometric origin of intraday variability. *Astron. Astrophys.* **255,** 59–62 (1992).
12. Ostorero, L., Villata, M. & Raiteri, C. M. Helical jets in blazars. Interpretation of the multifrequency long-term variability of AO 0235+16. *Astron. Astrophys.* **419,** 913–925 (2004).
13. Rieger, F. M. On the geometrical origin of periodicity in blazar-type sources. *Astrophys. J.* **615,** L5–L8 (2004).
14. Villata, M. *et al.* The correlated optical and radio variability of BL Lacertae. WEBT data analysis 1994–2005. *Astron. Astrophys.* **501,** 455–460 (2009).
15. Ghisellini, G. & Tavecchio, F. Canonical high-power blazars. *Mon. Not. R. Astron. Soc.* **397,** 985–1002 (2009).
16. Marcotulli, L. *et al.* High-redshift blazars through NuSTAR eyes. *Astrophys. J.* **839,** 96 (2017).
17. Mignone, A., Rossi, P., Bodo, G., Ferrari, A. & Massaglia, S. High-resolution 3D relativistic MHD simulations of jets. *Mon. Not. R. Astron. Soc.* **402,** 7–12 (2010).
18. Villata, M. *et al.* The unprecedented optical outburst of the quasar 3C 454.3. The WEBT campaign of 2004–2005. *Astron. Astrophys.* **453,** 817–822 (2006).
19. Raiteri, C. M. *et al.* Infrared properties of blazars: putting the GASP-WEBT sources into context. *Mon. Not. R. Astron. Soc.* **442,** 629–646 (2014).
20. Impey, C. D. & Neugebauer, G. Energy distributions of blazars. *Astron. J.* **95,** 307–351 (1988).
21. Malmrose, M. P., Marscher, A. P., Jorstad, S. G., Nikutta, R. & Elitzur, M. Emission from hot dust in the infrared spectra of gamma-ray bright blazars. *Astrophys. J.* **732,** 116 (2011).
22. Urry, C. M. & Padovani, P. Unified schemes for radio-loud active galactic nuclei. *Publ. Astron. Soc. Pacif.* **107,** 803–845 (1995).
23. Savolainen, T. *et al.* Relativistic beaming and gamma-ray brightness of blazars. *Astron. Astrophys.* **512,** A24 (2010).
24. Fromm, C. M. *et al.* Catching the radio flare in CTA 102. III. *Core-shift and spectral analysis. Astron. Astrophys.* **557,** A105 (2013).
25. Britzen, S. *et al.* A swirling jet in the quasar 1308+326. *Astron. Astrophys.* **602,** A29 (2017).
26. Perucho, M., Kovalev, Y. Y., Lobanov, A. P., Hardee, P. E. & Agudo, I. Anatomy of helical extragalactic jets: the case of S5 0836+710. *Astrophys. J.* **749,** 55 (2012).
27. Lyutikov, M. & Kravchenko, E. V. Polarization swings in blazars. *Mon. Not. R. Astron. Soc.* **467,** 3876–3886 (2017).

Acknowledgements This work used data from the Steward Observatory spectropolarimetric monitoring project. This programme is supported by NASA/Fermi Guest Investigator grant NNX15AU81G. We thank D. Oszkiewicz, J. Lehtinen, F. S. Kiaeerad, S. Geier, R. T. Rasmussen, P. B. Serrano and the NEON summer school students S. Tamburri, B. Hendricks, M. Smailagic and J. Laur for assistance with the NOT observations, and A. Carbognani for assistance with the OAVdA observations. This work is partly based on observations made with the Nordic Optical Telescope, operated by the Nordic Optical Telescope Scientific Association at the Observatorio del Roque de los Muchachos, La Palma, Spain, of the Instituto de Astrofisica de Canarias, and with telescopes IAC80 and TCS, which are operated by the Instituto de Astrofisica de Canarias in the Spanish Observatorio del Teide on the island of Tenerife. The IAC team acknowledges the assistance of the support astronomers and telescope operators of the Observatorio del Teide. This work is partly based on data obtained with the STELLA robotic telescopes in Tenerife, an AIP facility jointly operated by AIP and IAC. The Abastumani Observatory team acknowledges financial support by Shota Rustaveli NSF under contract FR/217950/16. O.M.K. acknowledges the financial support of the NSF of China under grant U1531245. The Kazakhstan team acknowledges financial support by the Ministry of Education and Science under grant numbers 0073-7/PSF and 0263/PSF. This research was partially supported by the Bulgarian National Science Fund of the Ministry of Education and Science under grant DN 08-1/2016. The Skinakas Observatory is a collaborative project of the University of Crete, the Foundation for Research and Technology–Hellas and the Max-Planck-Institut für Extraterrestrische Physik. The Boston University group acknowledges support from NSF grant AST-1615796. G.D. and O.V. acknowledge support from the Institute of Astronomy and Rozhen National Astronomical Observatory (Bulgarian Academy of Sciences) via the bilateral joint research project 'Observations of ICRF radio-sources visible in optical domain' (led by G.D.). This work is part of projects 176011 (Dynamics and kinematics of celestial bodies and systems), 176004 (Stellar physics) and 176021 (Visible and invisible matter in nearby galaxies: theory and observations), which are supported by the Ministry of Education, Science and Technological Development of the Republic of Serbia. This research was partially supported by the Bulgarian National Science Fund of the Ministry of Education and Science under grant DN 08-1/2016. The St Petersburg University team acknowledges support from Russian Science Foundation grant 17-12-01029. The AZT-24 observations were made within an agreement between the Pulkovo, Rome and Teramo observatories. The research at Ulugh Beg Astronomical Institute was supported by grant N. BA-FA-F-2-007 of the Uzbekistan Agency for Science and Technology. This work is partly based on observations carried out at the Observatorio Astronómico Nacional on the Sierra San Pedro Mártir (OAN-SPM), Baja California, Mexico. The Astronomical Observatory of the Autonomous Region of the Aosta Valley (OAVdA) is managed by the Fondazione Clément Fillietroz-ONLUS, which is supported by the Regional Government of the Aosta Valley, the Town Municipality of Nus and 'Unité des Communes valdôtaines Mont-Émilius'. This study is partly based on observations carried out with the IRAM 30-m, the Calar Alto 2.2-m and the Liverpool 2.0-m telescopes. The Calar Alto data were acquired as part of the MAPCAT project (http://www.iaa.es/~iagudo/_iagudo/MAPCAT.html). The IRAM data were acquired as part of the POLAMI project (http://polami.iaa.es). IRAM is supported by INSU/CNRS (France), MPG (Germany) and IGN (Spain). The Calar Alto observatory is jointly operated by MPIA (Germany) and IAA-CSIC (Spain). The Liverpool Telescope is operated by JMU with financial support from UK-STFC. I.A. acknowledges support by a Ramón y Cajal grant of Ministerio de Economía y Competitividad (MINECO) of Spain. The research at IAA–CSIC was supported in part by MINECO through grants AYA2016–80889–P, AYA2013–40825–P and AYA2010–14844, and by the regional government of Andalucía through grant P09–FQM–4784. This study used data obtained at the Metsähovi Radio Observatory, which is operated by Aalto University. The Submillimeter Array is a joint project of the Smithsonian Astrophysical Observatory and the Academia Sinica Institute of Astronomy and Astrophysics. This research used

NASA's Astrophysics Data System and the NASA/IPAC Extragalactic Database (NED), which is operated by the Jet Propulsion Laboratory, California Institute of Technology, under contract with the National Aeronautics and Space Administration. Part of this work is based on archival data, software or online services provided by the ASI Science Data Center (ASDC).

Author Contributions C.M.R. and M.V. managed the WEBT observing campaign, analysed the data, developed the geometric interpretation and wrote the manuscript. J.A.A.-P., A.A.A., M.I.C., N.C.-S., N.V.E., A.D.P., A.G., C.L., F.P., C.P., F.J.R.-L. and G.R.-C. performed near-infrared and optical observations and the related data reduction. I.A., C.C., A.F., J.L.G. and S.N.M. performed photometric and polarimetric optical and radio observations and the related data reduction. E.B., J.E., C.E., T.S.G., D.H., S.G.J., M.J., E.N.K., V.M.L., E.G.L., L.V.L., M.P.M., A.P.M., R.M., A.A.M., J.W.M., D.A.M., S.S.S., Yu.V.T., I.S.T. and A.A.V. acquired and reduced optical photometric and polarimetric data. R.B., G.V.B., G.A.B., V.B., M.S.B., P.C., D.C., W.-P.C., G.D., Sh.A.E., H.J., B.J., K.K., O.M.K., S.O.K., C.S.L., K.M., B.McB., B.Mi., M.M., D.O.M., S.V.N., M.G.N., J.M.O., D.N.O., E.O., T.A.P., N.R., K.S., A.C.S., M.R.S., E.S., B.A.S., L.S.-M., I.A.S., A.S. and O.V. carried out optical observations and the related data reduction. M.A.G., A.L., J.T., C.T. and M.T. performed radio observations and the related data reduction. W.B. acquired and reduced optical spectra. T.P. made optical photometric and spectroscopic observations and the related data reduction. P.S.S. carried out optical photometric, polarimetric and spectroscopic observations and reduced the data. F.D. and all the above authors reviewed and contributed to the manuscript.

Author Information Reprints and permissions information is available at www.nature.com/reprints. The authors declare no competing financial interests. Readers are welcome to comment on the online version of the paper. Publisher's note: Springer Nature remains neutral with regard to jurisdictional claims in published maps and institutional affiliations. Correspondence and requests for materials should be addressed to C.M.R. (raiteri@oato.inaf.it) or M.V. (villata@oato.inaf.it).

METHODS

Observations. Established in 1997, the WEBT Collaboration is an international collaboration of astronomers that monitor blazars in the optical, near-infrared, millimetre-wavelength and radio bands to investigate these highly active objects. Optical data used in this study were acquired at the following observatories: Abastumani (Georgia), AstroCamp (Spain), Belogradchik (Bulgaria), Calar Alto (Spain), Campo Imperatore (Italy), Crimean (Russia), Kitt Peak (USA), Lowell (USA; 70-cm, DCT and Perkins telescopes), Lulin (Taiwan), Michael Adrian (Germany), Mt Maidanak (Uzbekistan), New Mexico Skies (USA), Osaka Kyoiku (Japan), Polakis (USA), Roque de los Muchachos (Spain; Liverpool, NOT and TNG telescopes), ROVOR (USA), Rozhen (Bulgaria; 200- and 50/70-cm telescopes), San Pedro Martir (Mexico), Sirio (Italy), Skinakas (Greece), Steward (USA; Kuiper, Bok and Super-LOTIS), St Petersburg (Russia), Teide (Spain), Tien Shan (Kazakhstan), Tijarafe (Spain), Tucson (USA), Valle d'Aosta (Italy), Vidojevica (Serbia). The source magnitude was calibrated using common photometric standard stars in the source field (Star 1 and Star 2 in ref. 28, with the addition of other stars from ref. 29, when needed). This minimized possible offsets between different data sets. Observations were performed in the Johnson–Cousins *BVRI* bands, except for those at the NOT and Liverpool telescopes. The NOT data were obtained using the *ugriz* filters of the Sloan Digital Sky Survey and then converted with the transformations described in ref. 30. The Liverpool data were taken with the 'red' (770–1000 nm), 'green' (650–760 nm) and 'blue' (350–640 nm) cameras of the RINGO3 instrument and were transformed to the nearest standard (Johnson–Cousins) bands using shifts derived from data-taking periods overlapping with those of other instruments.

Near-infrared data were taken with the *JHK* filters at the Campo Imperatore, Lowell (Perkins) and Teide observatories. The data reduction is described in ref. 19.

Extended Data Fig. 1 shows the optical and near-infrared light curves of CTA 102 in the last four observing seasons. During the phases of the 2016–2017 outburst with the most dramatic variations, some episodes of noticeable and well-sampled intranight variability were observed. Four of them are shown in Extended Data Fig. 2.

Observations in the radio and millimetre-wavelength bands were performed with the 14-m radio telescope of the Metsähovi Radio Observatory (37 GHz) in Finland, the 30-m IRAM telescope (86 GHz and 230 GHz) in Spain and the Submillimetre Array (230 GHz) in Hawaii, USA. For details on the radio data analysis, see refs 31–33.

Spectral behaviour. The optical spectral behaviour of CTA 102 in the period of Extended Data Fig. 1 is shown in Extended Data Fig. 3, where the *B*–*R* colour indices (and the spectral slopes α of the $F \propto \nu^{-\alpha}$ law) are obtained by coupling data taken by the same telescope within 15-min intervals. A redder-when-brighter trend is observed until $R \approx 15$ (Spearman's rank correlation coefficient $\rho = -0.82$), which is followed by a slight bluer-when-brighter trend ($\rho = 0.26$) as the source flux increases. This has been previously reported[18] for 3C 454.3; it means that as the source brightens, the disk contribution becomes negligible and then the spectrum becomes bluer again, possibly because of changes in the Doppler factor[34]. In particular, we note that in faint states, when the source is 'blue', the brightness in the *B* band is much more stable than that in the *R* band. This means that the *B*-band flux is dominated by the disk emission, but the *R*-band flux still receives important synchrotron contribution from the jet, which makes the colour index vary considerably in these states.

Spectroscopic observations in the optical band were carried out at the Steward (Kuiper, Bok and MMT telescopes) and Roque de los Muchachos (TNG and NOT telescopes) observatories. A selection of these spectra is shown in Extended Data Fig. 4. The spectra taken during faint states show a prominent, broad Mg II emission feature and a hard spectral shape. As the brightness rises, the lines gradually disappear and the spectra soften as a consequence of the increasing importance of the featureless synchrotron continuum over the BBB. At the highest flux levels the optical spectra harden again, which is consistent with the bluer-when-brighter behaviour discussed earlier.

Modelling the thermal emission component. To model the BBB, whose contribution is assumed to remain constant throughout the observing period, we examined the flux variation ranges in the monitored bands. Figure 2 shows all the data acquired in the 2008–2017 period by WEBT observers in the radio–millimetre (37 GHz, 86 GHz and 230 GHz), near-infrared (*KHJ*) and optical (*IRVB*) bands. When passing from the observed magnitudes to the flux densities, we corrected for Galactic extinction using the recommendations of the NASA/IPAC Extragalactic Database. We built the SED of a hypothetical minimum-brightness synchrotron state by fitting a logarithmic parabolic model to the observed radio–millimetre minimum-flux densities and a minimum synchrotron flux density in the *K* band, which was obtained by assuming that the observed minimum-flux density in that band receives equal synchrotron and thermal contributions. The adequacy of a logarithmic parabolic model in describing the broadband synchrotron emission of blazars has been previously discussed (for example, in ref. 35), and this model is widely used. The thermal contribution from the BBB in all near-infrared and optical bands was then obtained by subtracting the model-predicted minimum synchrotron flux from the observed flux minima. The result is in agreement with that derived by ref. 19 for the same object using a quasi-stellar object template.

To complete the AGN model towards the mid–far infrared, we also added the emission contribution from the dust torus[19], although it is always negligible, except for the case when the source is very faint.

Relativistic beaming theory. The Doppler factor is defined as $\delta = [\Gamma(1-\beta\cos\theta)]^{-1}$, where β is the bulk velocity of the emitting source in units of the speed of light, $\Gamma = (1-\beta^2)^{-1/2}$ is the corresponding Lorentz factor and θ is the viewing angle. Any time interval is shortened in the observer's frame as $\Delta t = \Delta t'/\delta$, while frequencies are blueshifted as $\nu = \delta\nu'$ (primed symbols refer to quantities in the rest frame of the source). For a continuous jet with isotropic emission in the rest frame, the observed and rest-frame flux densities are linked by $F_\nu(\nu) = \delta^{2+\alpha} F'_{\nu'}(\nu)$, with $F'_{\nu'} \propto (\nu')^{-\alpha}$ (ref. 22). As a consequence, for a given beaming state characterized by a Doppler factor δ, the amplitude of the flux variation due to possible intrinsic processes is $\Delta F\nu \propto \delta^{2+\alpha}$. Therefore, stronger beaming enhances not only the flux but also the amplitude of the intrinsic variations (fast flares), and shortens the variation timescale. We can correct the observed flux densities at a given frequency for the variable Doppler beaming effect according to $F_\nu^{\rm cor} = F_\nu(\delta_\nu^{\rm const}/\delta_\nu^{\rm var})^{2+\alpha_\nu}$, where $F_\nu^{\rm cor}$ represents the values that we would observe if the jet had a constant orientation resulting in $\delta_\nu^{\rm const}$. In Fig. 3, we present $F_\nu^{\rm cor}$ in the *R* band for $\delta_\nu^{\rm const} = \delta_{\rm base}$.

Variation timescales. Inspection of the optical light curves reveals that variation timescales shorten when the source is brighter, which is a robust indication that the long-term flux changes are due to Doppler factor variations. This can be verified quantitatively by performing time-series analysis, that is, investigating the time structure of flux variations. In order to avoid possible bias due to the long-term trend and related difference in flux amplitude, we applied this analysis to flux densities corrected for the variable relativistic beaming effect (see Fig. 3). We separated the data set in two subsets corresponding to bright ($\delta > \delta_{\rm max}/2$) and faint ($\delta < \delta_{\rm max}/2$) states, thus separating the 2016–2017 outburst from the rest of the data. For the two subsets we calculated the structure function[36] (SF), which expresses the squared mean difference of the flux densities as a function of the time separation τ between data pairs. The results are shown in Extended Data Fig. 5, where the minimum variability timescale corresponds to the first peak of the SF, which is about 4 days for the bright states and approximately 8 days for the faint ones. This doubling of the timescales matches very well the δ-halving criterion adopted to separate the two subsamples ($\Delta t \propto \delta^{-1}$). We checked the SF results by means of the discrete autocorrelation function[37] (ACF; Extended Data Fig. 5b). The timescales are defined by the ACF minima. The shortest timescales for the high (low) flux states are confirmed to be about 4 (8) days.

Finally, we applied the Kolmogorov–Smirnov statistic to check whether the SFs and ACFs of the two subsamples are drawn from the same distribution. The values of the Kolmogorov–Smirnov statistic are 0.67 for the SFs and 0.39 for the ACFs with significance levels 1.1×10^{-6} and 1.0×10^{-4}, respectively; such small values mean that the two distributions are significantly different.

In view of these results and in agreement with the relativistic beaming theory, we modelled the optical long-term trend by setting an adaptive bin size that reduces the time bin by a factor n as the flux increases by a factor $n^{2+\alpha}$, where $n = 2, 3, 4, 5, 6, 7$ and $\alpha = 1.7$ is the slope of the minimum synchrotron spectrum in the *R* band.

Lorentz factor. We have assumed a single Γ value throughout the jet region of interest. Other scenarios, with Γ varying along or transversally to the jet are in principle possible and have been adopted in some cases. However, the portion of the jet that we are considering (that is, that emitting the bulk of photons from the optical band down to 37 GHz) is inside the inner core of the radio images, so that we can easily guess that the Lorentz factor does not change considerably along this region. On the other hand, transverse velocity gradients, for which there is no observational evidence in the inner zones of blazar jets, are sometimes introduced to explain the properties of high-energy, comptonized radiation[38,39], but they would represent an unnecessary complication for the purposes of our model.

Comparison between predicted and observed SEDs. The frequency-dependent trend of the Doppler factor, which is necessary to obtain a model SED for a given epoch, was derived by interpolating or extrapolating the values of δ at 37 GHz, 230 GHz and in the *R* band at that epoch (Fig. 3) in the δ–logν space, after correcting the frequencies for the different beaming affecting the base-level SED and the model SED for the considered epoch. We performed linear interpolation of the Doppler factor in the δ–logν space by minimizing the χ^2 error statistic. When the unreduced χ^2goodness-of-fit statistic was greater than 1.2, which indicates a poor fit, we also performed a parabolic interpolation and took the average fit

between the two. This occurred three times, for the epochs 7,637, 7,654 and 7,691 (in JD − 2,450,000).

Figure 2 displays ten SEDs that correspond to selected epochs spanning the source variation range. The predicted and observed SEDs are in very good agreement. In particular, the spectral slopes of the calculated SEDs in the optical band match very well those of the observed optical spectra. The offset between the optical and near-infrared data at epoch 7,717 is probably due to non-perfect simultaneity of the observations coupled with strong intranight variability. In Fig. 2, we also show the corresponding viewing angle as a function of frequency for all epochs. The brightest state during the 2016–2017 optical outburst corresponds to the maximum difference of orientation (maximum misalignment) between the radio- and optical-band emitting zones when the optical zone has the best alignment with the line of sight.

Polarization. Optical polarimetric data were acquired by seven observatories: Calar Alto, Crimean, Lowell (Perkins), ROVOR, San Pedro Martir, Steward and St Petersburg. The temporal behaviour of the jet polarization fraction $P_{\rm jet}$ and electric vector polarization angle (EVPA) are shown in Extended Data Fig. 6.

$P_{\rm jet}$ was obtained from the observed polarization degree P by correcting for the dilution effect of the unpolarized BBB emission, $P_{\rm jet} = P \times F/F_{\rm jet}$, where F is the de-absorbed flux density and $F_{\rm jet}$ is the same quantity after subtraction of the BBB flux contribution. Extended Data Fig. 6 also shows the mean value of $P_{\rm jet}$ for the whole period and the mean values and standard deviations for each observing season. The EVPA was adjusted for the $\pm n \times \pi$ (n, natural number) ambiguity by requiring that the angle difference between subsequent points in the same observing season is minimum.

Strong variability of $P_{\rm jet}$ and large changes of the EVPA both in the clockwise and anticlockwise directions are observed throughout the period considered. No general correlation is found with the observed flux or with the flux variations that remain after correction for variable Doppler beaming (see Fig. 3). The only hint of correlation between polarization and flux variations is given by the coincidence of the minima in the viewing angle (flux peaks) with either fast changes of the EVPA (at JD ≈ 2,457,300) or inversion of its direction (at JD ≈ 2,456,200 and JD ≈ 2,457,750; that is, during the peaks of the 2012[9,10] and 2016–2017 outbursts). Both situations may occur when considering a rotating helical jet with a longitudinal magnetic field. As the helix rotates and the emitting region approaches the line of sight, the EVPA undergoes large variations or changes of direction, depending on whether the angle between the line of sight and the helix axis is smaller or larger than the helix pitch angle, respectively. However, some turbulence must be present[5] to explain the irregular behaviour of $P_{\rm jet}$. An alternative explanation could be provided by ref. 27, which showed that apparent random behaviour of P (and F) can accompany large EVPA fluctuations in a jet with a helical magnetic field and variable propagation direction.

Comparison with a standard one-zone model. We have shown that the long-term multiwavelength flux variability of CTA 102 is well explained by changes of the Doppler factor. We now investigate whether commonly used one-zone models can also explain these spectral changes in the same way. In Extended Data Fig. 7 we present results obtained with the standard one-zone model, proposed in ref. 40. We first fitted the SED at JD = 2,457,637, which represents an intermediate flux level. We used the following physical parameters: radius of the emitting zone $\log[R\ ({\rm cm})] = 17.8$; magnetic field $B = 0.08$ G; Doppler factor $\delta = 21.5$; electron density in the emitting zone $N = 30\ {\rm cm}^{-3}$; electron energies between $\log\gamma_{\rm min} = 1$ and $\log\gamma_{\rm max} = 5$; and an electron energy distribution expressed by a power law with $\alpha = 2.15$ and a cut-off electron energy $\log\gamma_{\rm cut} = 3.6$.

We then tried to fit the highest and the lowest optical levels shown in Fig. 2 by changing only δ. The brightest state requires $\delta = 40$ and the faintest $\delta = 9.5$. However, this model does not fit the lower-frequency data; in particular, the flux in the millimetre-wavelength band is largely over- or under-estimated. Better fits could be obtained with the one-zone model, but at the cost of changing a number of parameters, especially the electron energy distribution. One should then check if a reasonable temporal evolution of all these parameters can be found to explain the multiwavelength light curves.

Data availability. Data taken and assembled by the WEBT Collaboration (optical, near-infrared and radio light curves) are stored in the WEBT archive at the Osservatorio Astrofisico di Torino, INAF (http://www.oato.inaf.it/blazars/webt/); they become publicly available one year after publication and can be requested from the WEBT President, M.V. (villata@oato.inaf.it). Optical spectropolarimetric data from the Steward Observatory are publicly available and can be downloaded from http://james.as.arizona.edu/~psmith/Fermi/.

28. Raiteri, C. M., Villata, M., Lanteri, L., Cavallone, M. & Sobrito, G. *BVR* photometry of comparison stars in selected blazar fields. II. Photometric sequences for 9 quasars. *Astron. Astrophys. Suppl. Ser.* **130,** 495–500 (1998).
29. Doroshenko, V. T. *et al.* BVRI CCD-photometry of comparison stars in the fields of galaxies with active nuclei. V. *Astrophysics* **56,** 343–358 (2013).
30. Jordi, K., Grebel, E. K. & Ammon, K. Empirical color transformations between SDSS photometry and other photometric systems. *Astron. Astrophys.* **460,** 339–347 (2006).
31. Teräsranta, H. *et al.* Fifteen years monitoring of extragalctic radio sources at 22, 37 and 87 GHz. *Astron. Astrophys. Suppl. Ser.* **132,** 305–331 (1998).
32. Agudo, I., Thum, C., Wiesemeyer, H. & Krichbaum, T. P. A. 3.5 mm polarimetric survey of radio-loud active galactic nuclei. *Astrophys. J. Suppl. Ser.* **189,** 1–14 (2010).
33. Gurwell, M. A., Peck, A. B., Hostler, S. R., Darrah, M. R. & Katz, C. A. Monitoring phase calibrators at submillimeter wavelengths. In *From Z-Machines to ALMA: (Sub)Millimeter Spectroscopy of Galaxies (ASP Conf. Ser. 375)* (eds Baker, A. J. *et al.*) 234–237 (Astronomical Society of the Pacific, 2007).
34. Larionov, V. M., Villata, M. & Raiteri, C. M. The nature of optical and near-infrared variability of BL Lacertae. *Astron. Astrophys.* **510,** A93 (2010).
35. Massaro, E., Perri, M., Giommi, P. & Nesci, R. Log-parabolic spectra and particle acceleration in the BL Lac object Mkn 421: Spectral analysis of the complete BeppoSAX wide band X-ray data set. *Astron. Astrophys.* **413,** 489–503 (2004).
36. Simonetti, J. H., Cordes, J. M. & Heeschen, D. S. Flicker of extragalactic radio sources at two frequencies. *Astrophys. J.* **296,** 46–59 (1985).
37. Hufnagel, B. R. & Bregman, J. N. Optical and radio variability in blazars. *Astrophys. J.* **386,** 473–484 (1992).
38. Ghisellini, G., Tavecchio, F. & Chiaberge, M. Structured jets in TeV BL Lac objects and radiogalaxies Implications for the observed properties. *Astron. Astrophys.* **432,** 401–410 (2005).
39. Sikora, M., Rutkowski, M. & Begelman, M. C. A spine-sheath model for strong-line blazars. *Mon. Not. R. Astron. Soc.* **457,** 1352–1358 (2016).
40. Tramacere, A., Giommi, P., Perri, M., Verrecchia, F. & Tosti, G. Swift observations of the very intense flaring activity of Mrk 421 during 2006. I. Phenomenological picture of electron acceleration and predictions for MeV/GeV emission. *Astron. Astrophys.* **501,** 879–898 (2009).

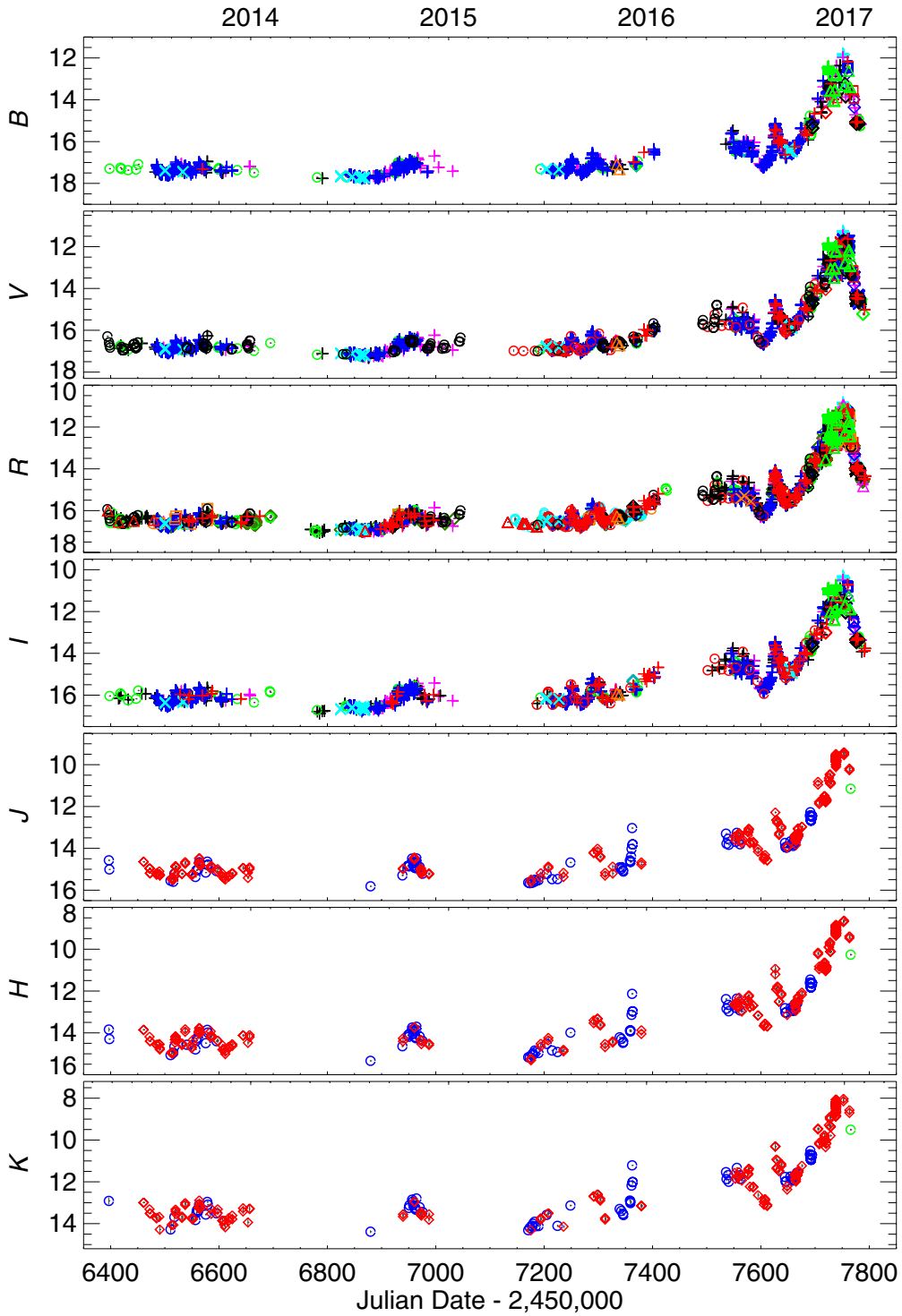

Extended Data Figure 1 | Observed light curves of CTA 102 in the optical *BVRI* and near-infrared *JHK* bands. The curves are built with data from 39 telescopes (marked with different symbols and colours) in 28 observatories participating in the WEBT project. Measurement errors (1 s.d.) are smaller than the symbol size.

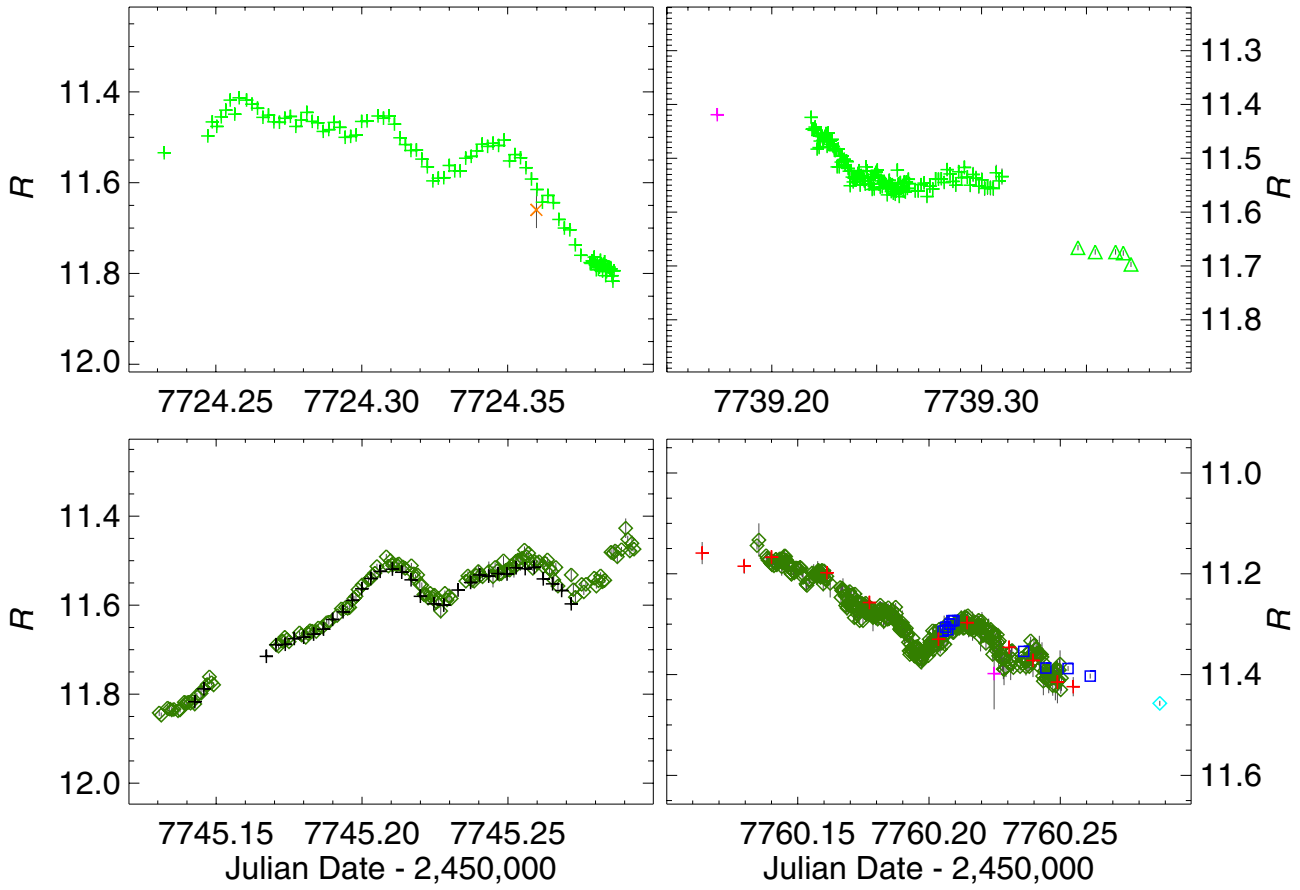

Extended Data Figure 2 | Four episodes of noticeable and well-sampled intranight variability. Magnifications of the *R*-band light curve of Fig. 1 during the phases of the 2016–2017 optical outburst with the most dramatic changes reveal very fast brightness variations. Error bars represent 1 s.d. measurement errors.

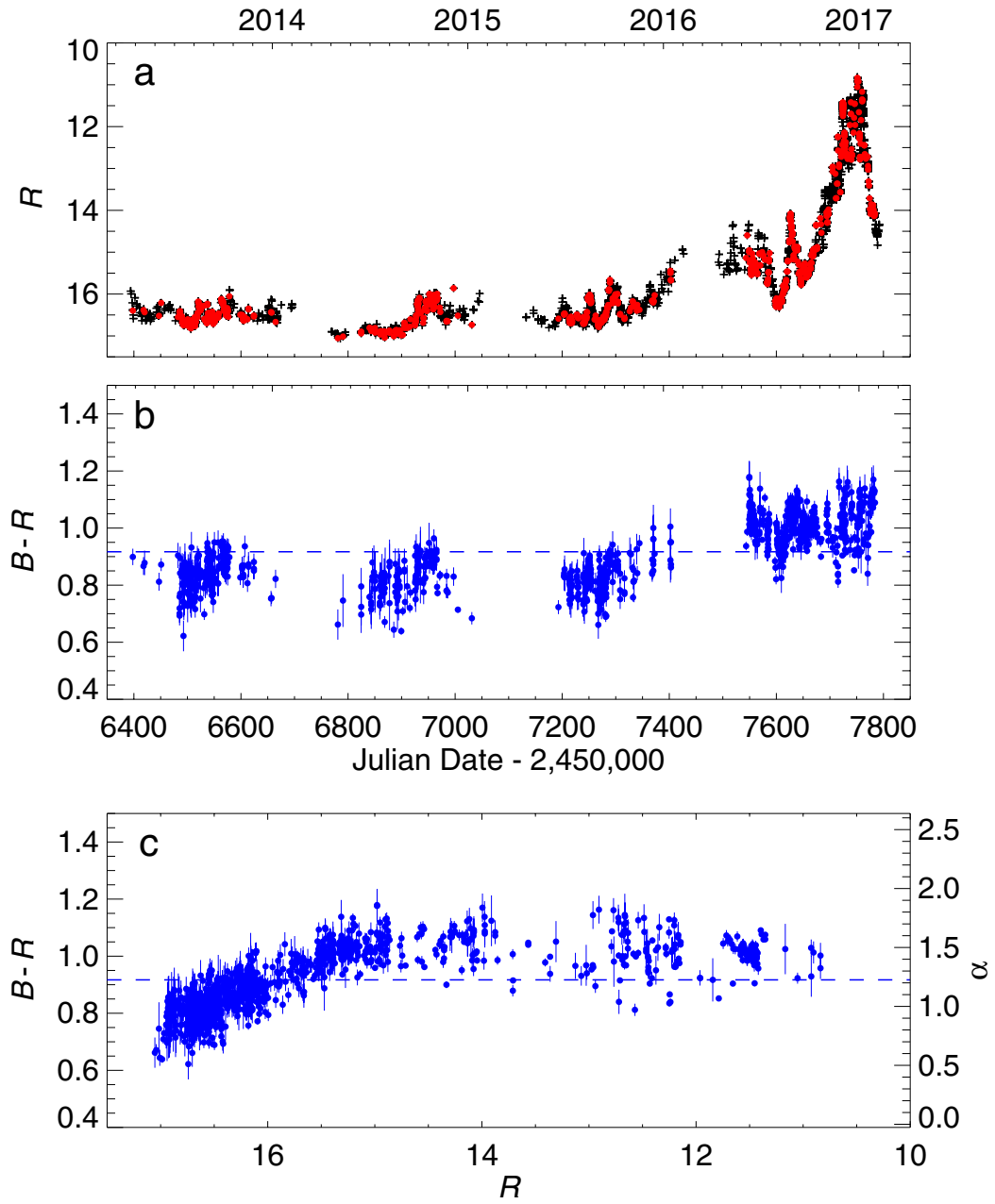

Extended Data Figure 3 | Colour behaviour of CTA 102. a, The *R*-band light curve; red dots represent the data points used to build the colour indices. **b–c**, The $B-R$ colour index as a function of time and *R*-band magnitude. Error bars were obtained by summing in quadrature the 1-s.d. measurement errors of the corresponding *B* and *R* data. The dashed line indicates the average $B-R$ value. The parameter α is the spectral index of the $F \propto \nu^{-\alpha}$ law. The redder-when-brighter trend that characterizes faint source states ($R > 15$) turns into a slight bluer-when-brighter trend as the source flux increases.

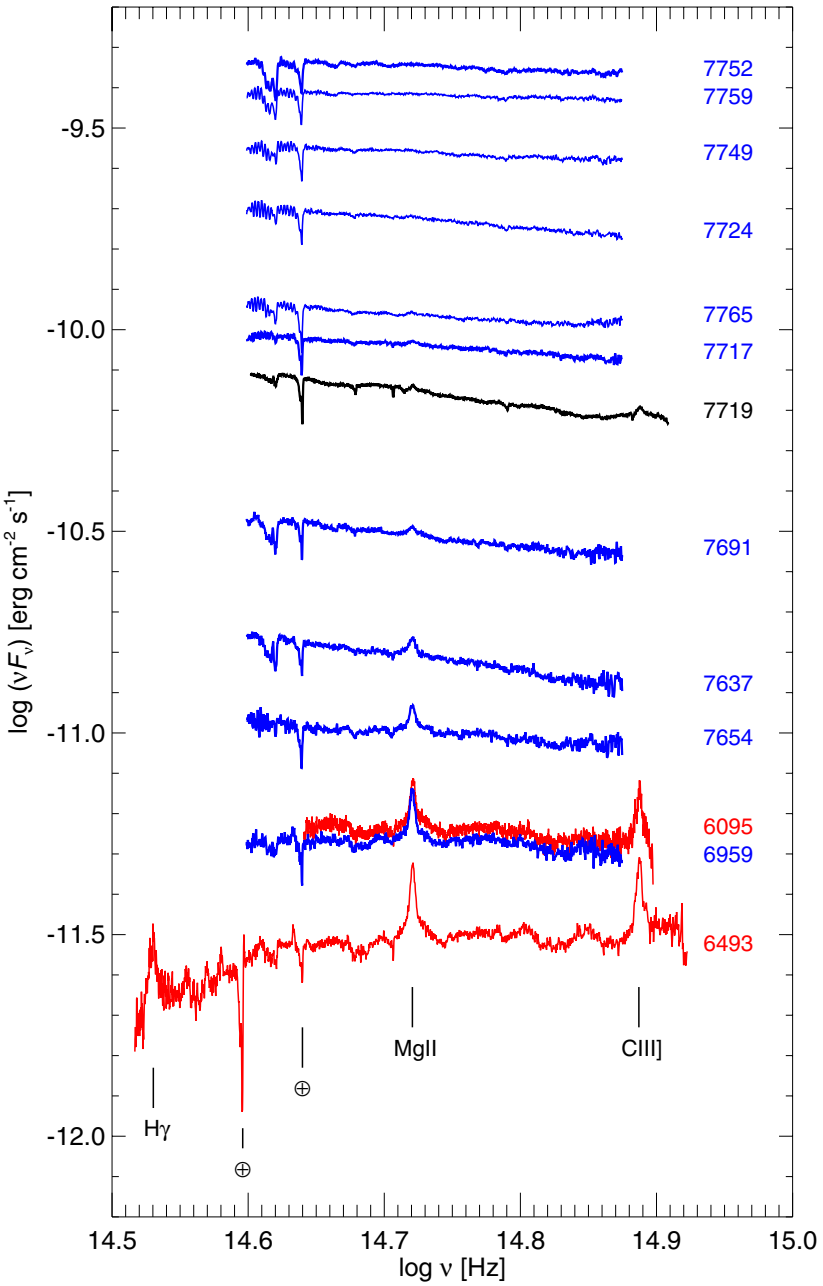

Extended Data Figure 4 | Optical spectra of CTA 102 in different brightness states. Data are from the Steward (blue) and Roque de los Muchachos (TNG and NOT; black and red, respectively) observatories and have been corrected for Galactic extinction. The observing epochs are given on the right, expressed in JD − 2,450,000. The main broad emission lines (more visible in faint states) are indicated. As the flux increases, the source spectrum first softens (redder-when-brighter trend) and then gradually hardens (bluer-when-brighter).

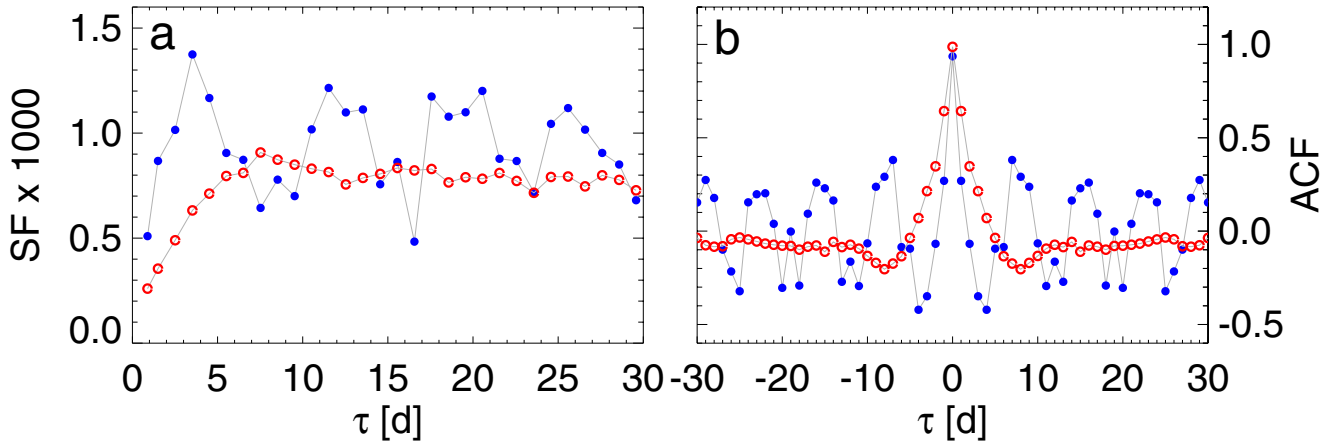

Extended Data Figure 5 | Results of time-series analysis on the optical fluxes. a, Structure function of *R*-band flux densities, corrected for the long-term trend due to variable relativistic beaming (see Fig. 3). **b**, Autocorrelation function of the same corrected fluxes. τ is the time separation between points, expressed in 1-day bins. Filled blue and empty red symbols refer to bright (more beamed) and faint (less beamed) observed states, respectively, and show that variation timescales are halved when the Doppler factor doubles.

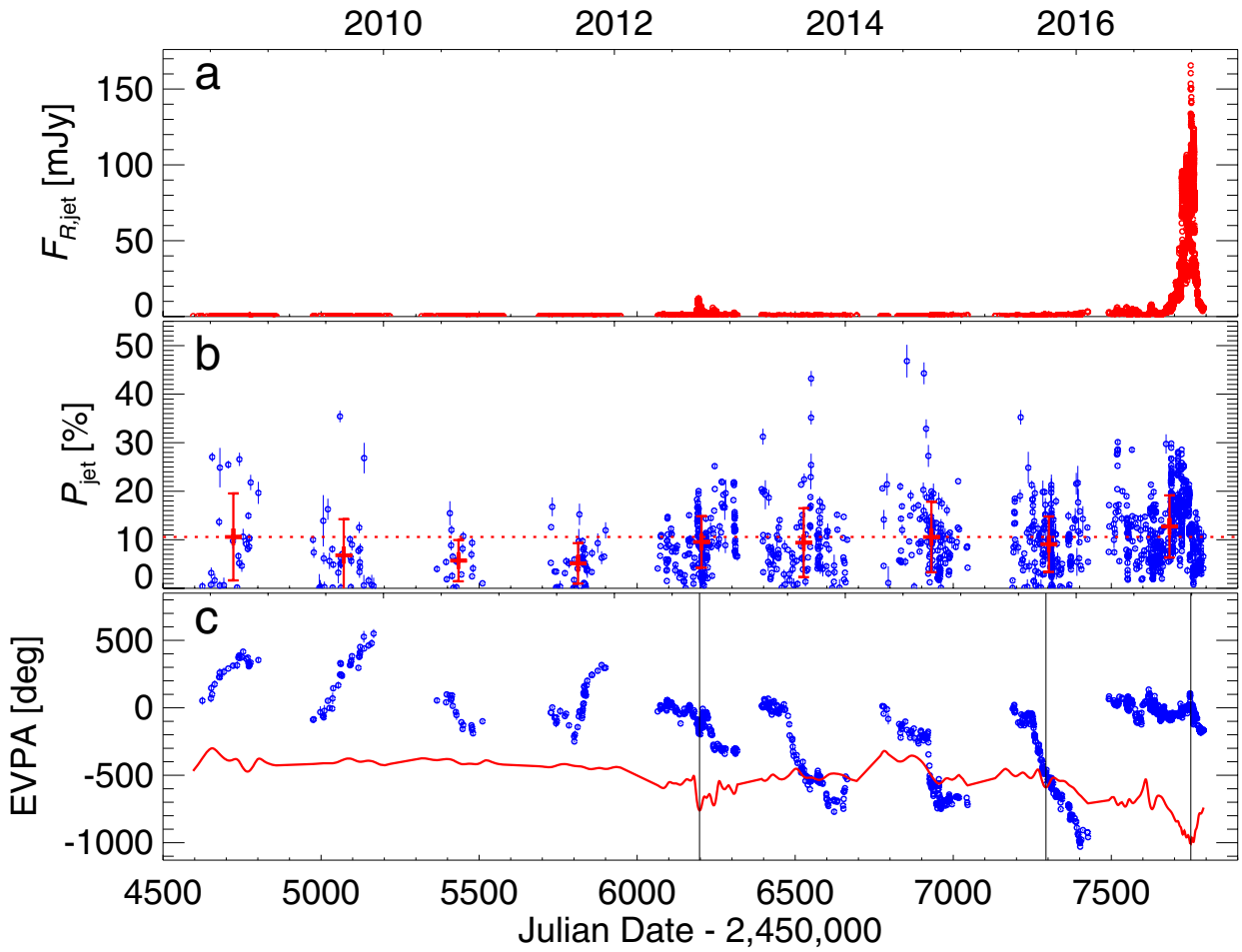

Extended Data Figure 6 | Temporal behaviour of the polarization of CTA 102. a, The jet optical flux densities. **b**, The jet polarization fraction P_{jet}. The horizontal dotted line indicates the average value over the whole period and crosses show the mean values in each observing season. Error bars represent 1 s.d. **c**, The electric vector polarization angle. The red solid line displays the trend of the viewing angle in the *R* band (rescaled to fit in the plot; see Fig. 3) and the vertical lines mark the most interesting events, which are discussed in the text.

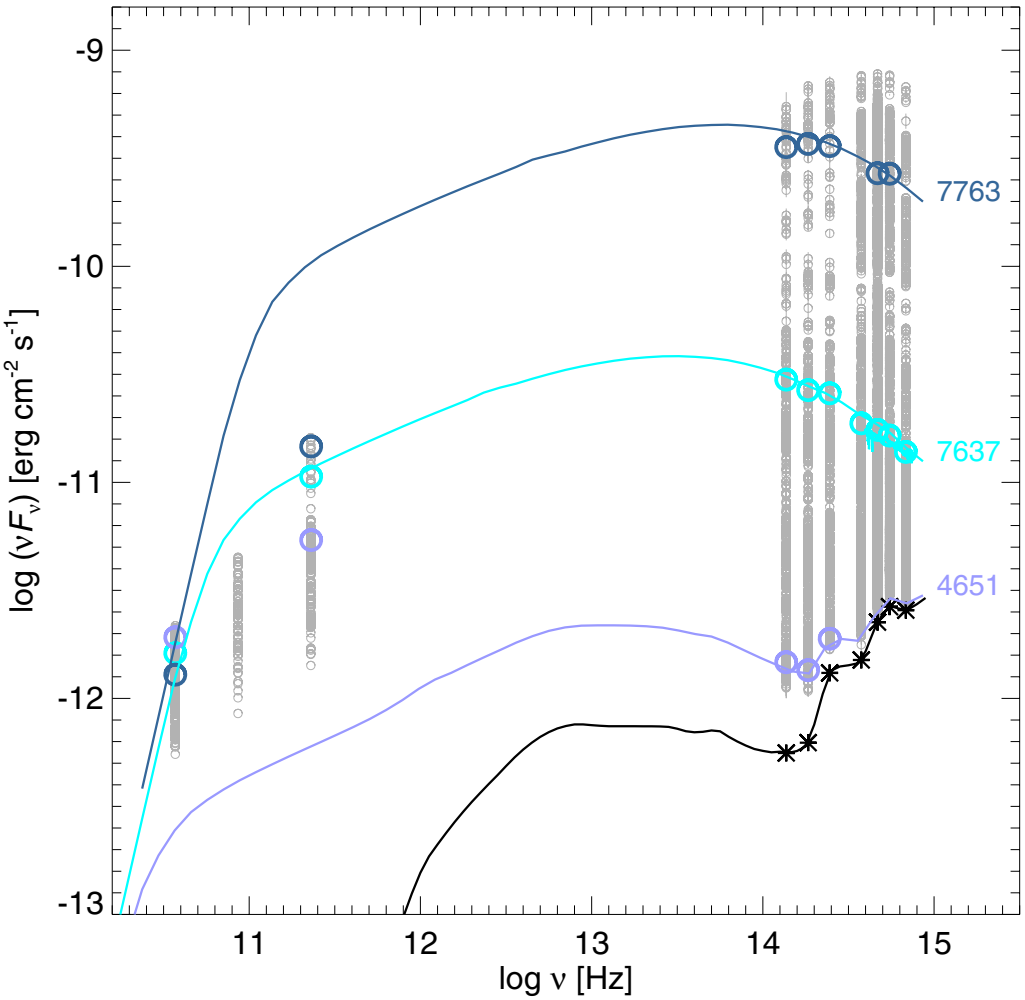

Extended Data Figure 7 | One-zone model fits to the SEDs of CTA 102. The standard one-zone model[40] has been used to fit three SEDs in intermediate-, high- and low-brightness states (see also Fig. 2). Once the physical parameters of the emitting zone are adjusted to reproduce the intermediate-brightness state, the other two model fits are obtained by changing only the Doppler factor to match the optical data. As a result, the millimetre-wavelength flux is largely over- or under-estimated. In all model fits, the thermal component (accretion disk and torus; black line and symbols) was added to the one-zone model synchrotron component.

Author Queries

Journal: **Nature**
Paper: **nature24623**
Title: **Blazar spectral variability as explained by a twisted inhomogeneous jet**

Query Reference	Query
1	AUTHOR: A PDF proof has been produced on the basis of your corrections to the preproof and contains the main-text figures edited by us and the Extended Data items supplied by you (which may have been resized but will not have been edited otherwise by us). Please check that the display items are as follows (doi:10.1038/nature24623): Figs 1, 2, 3, 4 (all colour); Tables, none; Boxes, none; Extended Data display items, 7; SI, no. Please check the edits to all main-text figures (and tables, if any) very carefully, and ensure that any error bars in the figures are defined in the figure legends. If you wish to revise the Extended Data items for consistency with main-text figures and tables, please copy the style shown in the PDF proof (such as italicising variables and gene symbols, and using initial capitals for labels) and return the revised Extended Data items to us along with your proof corrections.
2	AUTHOR: This date will be confirmed by the proofreader.
3	AUTHOR: If the paper fits in four pages on proof, then we can keep the Acknowledgments section here. Otherwise, we will move it to Supplementary Information.
Web summary	The spectral variability of the blazar CTA 102 during a recent extreme outburst could be explained by a twisted, inhomogeneous jet containing regions of different orientations that vary in time

For Nature office use only:

Layout	☐	Figures/Tables/Boxes	☐	References	☐
DOI	☐	Error bars	☐	Supp info	☐
Title	☐	Colour	☐	Acknowledgements	☐
Authors	☐	Text	☐	Author contribs	☐
Addresses	☐	Methods	☐	COI	☐
First para	☐	Received/Accepted	☐	Correspondence	☐
		AOP	☐	Author corrx	☐
		Extended Data	☐	Web summary	☐
				Accession codes link	☐
				Referee accreditation	☐

SUBJECT WORDS
Physical sciences/Astronomy and planetary science/Astronomy and astrophysics/High-energy astrophysics [URI /639/33/34/864];
Physical sciences/Astronomy and planetary science/Astronomy and astrophysics/Galaxies and clusters [URI /639/33/34/863].

TECHNIQUE TERMS
Not Applicable.